PAPER

Check for updates

Three-dimensional hierarchical ZnCo$_2$O$_4$@C$_3$N$_4$-B nanoflowers as high-performance anode materials for lithium-ion batteries†

Haihong Xiao, [ID] Guoqing Ma, Junyu Tan, Shuai Ru, [ID] Zhaoquan Ai* and Caixia Wang*

ZnCo$_2$O$_4$ has become one of the most widely used anode materials due to its good specific capacity, cost-efficiency, high thermal stability and environmental benignity. However, its poor conductivity and cycle stability have limited its practical application in lithium-ion batteries. To overcome these issues, we constructed a 3D nanoflower composite material (ZnCo$_2$O$_4$@C$_3$N$_4$-B) by combining ZnCo$_2$O$_4$ as a framework and B-doped g-C$_3$N$_4$ (g-C$_3$N$_4$-B) as a new carbon source material *via* a simple hydrothermal method. ZnCo$_2$O$_4$@C$_3$N$_4$-B exhibited exceptional specific capacitance of 919.76 mA h g^{-1} after 500 cycles at 0.2 A g^{-1} and a long-term capacity retention of 97.8% after 1000 cycles at 2 A g^{-1}. The high reversible capacity, long cycling life and good rate performance could be attributed to the 3D interconnected architecture and doping of g-C$_3$N$_4$-B. This work provides a simple and general strategy to design high-performance anode materials for lithium-ion batteries to meet the needs of practical applications.

1. Introduction

Rechargeable lithium-ion batteries (LIBs) have been utilized widely as the main choice for mobile terminal equipment and electric vehicles.[1–3] Transition metal oxides have become the preferred next-generation selectable materials for lithium-ion battery anodes due to their high specific capacity.[4,5] Among these transition metal oxides, the binary transition metal oxides AB$_2$O$_4$ with a spinel structure can not only overcome the shortcomings of the large first-discharge capacity loss and poor cyclic stability of simple metal oxides by using the compounding principle and taking advantage of properties of multiple components, but also have attracted growing attention owing to their synergistic effect on various action mechanisms.[6] Especially relative to other binary transition metal oxides, ZnCo$_2$O$_4$ with good specific capacity, cost-efficiency, high thermal stability and environmental benignity has become one of the most widely studied materials.[7] Simultaneously, as a binary metal oxide, it has two reaction mechanisms of insertion and conversion in the electrode reaction, which improve and counteract the problem of electrochemical performance

Hubei Collaborative Innovation Center for Advanced Organic Chemical Materials, Ministry of Education Key Laboratory for the Synthesis and Application of Organic Functional Molecules, College of Chemistry and Chemical Engineering, Hubei University, Wuhan 430062, P. R. China. E-mail: 1045065959@qq.com; 2326978832@qq.com

† Electronic supplementary information (ESI) available: Supplementary figures of electrochemical performances. See DOI: 10.1039/d0ra05203e

degradation common with single metal oxides.[34–36] However, its poor conductivity and cycle stability have limited its practical application in LIBs.[8,9]

In order to improve the electrochemical performance of the material, researchers have increased the specific surface area of the material by changing its morphology, such as nanospheres,[10] nanotubes[11] and nanosheets,[12,13] but the requirement for precise control of morphology in the process of experimental synthesis can limit the wide application of the material. Therefore, it is important to develop an easy, general and environmentally benign process for the synthesis of 3D hierarchical ZnCo$_2$O$_4$ for electrode materials.

The other effective method is to synthesize transition metal oxide composites doped with a carbon material that can effectively alleviate the volume expansion by adjusting the 2D/3D network matrix.[14,15] Graphene nanosheets with good conductivity and large specific surface area are often used as the carbon source, but their low theoretical specific capacity (372 mA h g^{-1}) and high cost limit their pervasive application.[16] In recent years, graphite-like materials have gradually replaced graphene materials because of their simple preparation processes and low cost.[17] Among these, g-C$_3$N$_4$ has emerged as a promising carbon source of anode materials owing to its many advantages, such as excellent thermal and chemical stability, environmental friendliness, many preparation methods and easy access.[18,19]

Moreover, in the field of electrocatalysis and photocatalysis, doping non-metals and metals in g-C$_3$N$_4$ is an effective strategy to enhance the catalytic activity. Non-metal-doping materials, such as B-doped and S-doped g-C$_3$N$_4$, have been reported to

enhance both the photocatalytic and electro-catalytic activity of g-C_3N_4.[20] Moreover elemental doping can readily tune the band gap structure of g-C_3N_4, facilitating the separation and transfer of electron–hole pairs at the heterojunction interface.[21] Therefore, B-doped and S-doped g-C_3N_4 may be used as a new carbon source material to improve the electrochemical performance of the electrode.

Inspired by the fascinating electrocatalytic performances of ion-doped g-C_3N_4 materials, B-doped or S-doped g-C_3N_4 as a new carbon source material was used to construct a modified $ZnCo_2O_4$@C_3N_4 hybrid anode material by a simple hydrothermal method. Interestingly, nanosphere, nanosheet and nanoflower composite materials of $ZnCo_2O_4$ and modified graphene-like materials were obtained by doping g-C_3N_4, g-C_3N_4-S and g-C_3N_4-B, respectively. Also, the morphology has a great effect on the electrochemical performance of the anode materials. The g-C_3N_4-B doped $ZnCo_2O_4$ nanoflower composite materials (ZCO@C_3N_4-B) showed a high reversible capacity, long cycling life and good rate performances due to large surface area and g-C_3N_4-B doping. Given these advantageous of this composite, it provides a simple and effectual method for manufacturing high-performance anodes for lithium-ion batteries, especially in practical use.

2. Experimental

2.1 Materials and instrumentations

Melamine, boric acid, thiourea, PVP, $Zn(CH_3COOH)_2 \cdot 2H_2O$ and $Co(CH_3COOH)_2 \cdot 4H_2O$ were obtained from Shanghai Chemical Co. The microstructures and morphologies of the samples were characterized by scanning electron microscopy (SEM, JSM-6510LV) and high-resolution transmission electron microscopy (HRTEM, Tecnai G20). The crystallographic structure was examined by X-ray diffraction (XRD, D8-ADVANCE) and Raman spectrometry (NEXUS670). Surface analysis of the samples was carried out by X-ray photoelectron spectroscopy (XPS, Escalab 250X, Thermo Fisher Scientific). The surface area measurements were performed according to the Brunauer–Emmett–Teller (BET, 3H-2000A) method.

2.2 Electrochemical measurements

Electrochemical performances were measured using coin cells (LIR 2025) assembled in a glove box filled with argon. The electrode was prepared with 80 wt% of the composite materials (ZCO@C_3N_4, ZCO@C_3N_4-S or ZCO@C_3N_4-B), 10 wt% carbon black, and 10 wt% sodium carboxymethyl cellulose (CMC). The electrolyte consisted of a solution of 1 M $LiPF_6$ in EC/DEC (1 : 1, v/v). Galvanostatic tests of the assembled cells were carried out using a Xinwei (BTS7.6.x 5 V/50 mA) system in the voltage range of 0.01–3.0 V (vs. Li^+/Li). Cyclic voltammetry (CV) characteristics of the samples were analyzed within the potential range between 0.01–3.0 V at a scanning speed of 0.1 mV s^{-1} on a Shanghai Chenhua electrochemical workstation (CHI 600E). Also, electrochemical impedance spectroscopy (EIS) characterization was also performed on cells assembled with active

materials at a testing frequency of 0.01 Hz to 100 kHz at room temperature.

2.3 Sample preparation

Syntheses of g-C_3N_4, g-C_3N_4-S and g-C_3N_4-B. The g-C_3N_4-B was synthesized by the template method. Melamine (1 g), boric acid (1 g) and NaCl (1 g) were dissolved in 30 ml ethanol solution. The mixture was stirred, the solvent evaporated off at 80 °C, and the remaining material was ground and then transferred to a ceramic crucible with a lid to calcine in a tube furnace for 4 h under argon conditions at 550 °C. After being washed and peeled off, the mixture was dried at 80 °C to obtain g-C_3N_4-B. The g-C_3N_4-S material was synthesized by the same experimental method and procedure. Replacing boronic acid by thiourea. g-C_3N_4 was prepared by directly pyrolyzing melamine by the same procedure.

Syntheses of ZCO@C_3N_4, ZCO@C_3N_4-S and ZCO@C_3N_4-B. PVP (1 g) was dissolve in ethylene glycol (30 ml) and stirred at room temperature for 2 h. The $Zn(CH_3COOH)_2 \cdot 2H_2O$ (2 mmol) and $Co(CH_3COOH)_2 \cdot 4H_2O$ (4 mmol) were added to the solution and stirred for 30 min. The graphene-like material (g-C_3N_4, g-C_3N_4-S or g-C_3N_4-B) (0.2 g) was dissolved in 30 ml ethylene glycol with sonicating for 30 min, and then transferred into the above solution. The mixed solution was kept at 180 °C for 16 h in a Teflon-lined stainless steel autoclave. After the solution was cooled to room temperature, the product was collected by centrifugation, washed several times with distilled water and ethanol, and then dried at 80 °C for 24 h to remove water. The brown powder was collected, ground with a mortar and pestle, and then annealed in an argon atmosphere at 400 °C for 2 h at a heating rate of 2 °C min^{-1}. Finally, the product (ZCO@C_3N_4, ZCO@C_3N_4-S and ZCO@C_3N_4-B) was obtained.

3. Results and discussion

3.1 Synthesis and characterization

As schematically illustrated in Fig. 1, the ZCO@C_3N_4-B sample was synthesized via the following steps. First, the g-C_3N_4-B carbon source materials were synthesized by template calcination using NaCl, $C_3H_6N_6$ and H_3BO_3. Afterwards, using PVP as

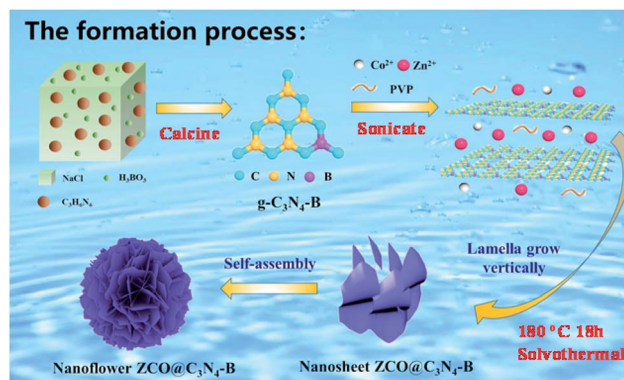**Fig. 1** Schematic illustration of the synthesis of the 3D nanoflower ZCO@C_3N_4-B.

the surface stabilizer, $Zn(CH_3COOH)_2$ and $Co(CH_3COOH)_2$ as the zinc source and cobalt source, respectively, g-C_3N_4-B was used as the carbon source for ultrasonic dispersion and the precursor was synthesized by the solvent heat method. Finally, the product ZCO@C_3N_4-B was obtained by calcining the precursor under the condition of 400 °C argon gas. Meanwhile, the sample ZCO@C_3N_4-S adopted the same operation process, except that boric acid was replaced by thiourea, while the ZCO@C_3N_4 sample only uses C_3N_4 as the carbon source for comparison. The morphologies of the composite materials strongly depended on the doping carbon materials, which had a great effect on the electrochemical performance of the anode material.

X-ray diffraction (XRD) analysis was used to determine the crystalline phase of the sample. As shown in the Fig. 2(a), strong characteristic diffraction peaks of the graphene-like materials (g-C_3N_4, g-C_3N_4-S and g-C_3N_4-B) were observed at 24.23° and 43.51°, which were attributed to the (002) and (100) crystal planes of graphite.[22] The graphitization degree of the g-C_3N_4 graphene materials was low. After doping the S and B elements, the corresponding peak diffraction angle of the (002) crystal plane was closer to 26° of the pure graphite crystal and the diffraction intensity was increased remarkably.[23] These results demonstrated that the degree of graphitization of the composite materials was enhanced after doping with the S or B element. Also, Fig. 2(b) displays the diffraction patterns of the ZCO@C_3N_4, ZCO@C_3N_4-S and ZCO@C_3N_4-B composites materials. The diffraction peaks of those materials were located at 18.96°, 31.22°, 36.81°, 38.49°, 44.74°, 55.57°, 59.28°, 65.15°, 74.00° and 77.22°, corresponding to the crystal faces (111), (220), (311), (222), (400), (422), (511), (440), (620) and (533) of cubic $ZnCo_2O_4$ with a typical spinel structure (JCPDS Card No. 23-1390).[24] No other impurity peaks were observed. This indicated that all of the composite materials had an excellent crystallization degree. Also, doping with B and S elements increased the peak strength, suggesting the formation of more

stable crystal structures of the ZCO@C_3N_4-B and ZCO@C_3N_4-S. The absence of carbon peaks showed that graphene-like materials had been graphitized.[25]

Raman spectroscopy was performed to study the structural properties of the composite materials. As shown in Fig. 2(c), all the samples had three peaks at 473, 512 and 654 cm^{-1}, respectively. The peaks at 473 cm^{-1} from the stretching vibration of Zn–O and Co–O bond were attributed to the active mode E_g. The characteristic peak at 512 cm^{-1} was from the vibration of the Co–O bond, corresponding to a symmetric mode of F_{2g}. Also, the expansion vibration of the Co–O bond at 654 cm^{-1} was ascribed to the vibration mode of A_{1g}.[26] The D peak (1357 cm^{-1}) was the disordered vibration peak of graphitic carbon, and the G peak (1584 cm^{-1}) was the in-plane vibration peak of the carbon atom sp^2. The relative dimensional intensity I_D/I_G ($R = I_D/I_G$) reflected the degree of carbonization of the material. The R values of ZCO@C_3N_4, ZCO@C_3N_4-S, and ZCO@C_3N_4-B were 0.87, 0.84, and 0.82, respectively. After doping with B and S elements, the R values decreased. Also, the R value of ZCO@C_3N_4-B was smaller than that of ZCO@C_3N_4-S, indicating the higher degree of carbonization of ZCO@C_3N_4-B.

In order to further analyze the specific surface area and pore size of the sample, the adsorption and desorption isotherms of the ZCO@C_3N_4, ZCO@C_3N_4-S and ZCO@C_3N_4-B samples were tested by N_2. As shown in Fig. 2(d), all three materials conformed to type IV and the mesoporous hysteresis loop belonged to type H3, which may lead to an inconspicuous saturated adsorption platform due to the irregular mesoporous structure of the material.[28] The formula of the multi-molecule layer adsorption was derived from BET theory:[29] the specific surface area of the ZCO@C_3N_4-B sample was calculated to be 137.02 cm^3 g^{-1} (ZCO@C_3N_4-S and ZCO@C_3N_4 were 63.27 and 27.86 cm^3 g^{-1}, respectively), and the pore size (shown in the ESI Fig. S5†) was mainly distributed between 9–12 nm (ZCO@C_3N_4-S and ZCO@C_3N_4 were between 15–18 nm and 42–50 nm, respectively). It could be clearly seen that the specific surface area of the ZCO@C_3N_4-B sample was greater than that others. However, this was mainly attributed to the layer with the nanoflower structure being beneficial to increase the specific surface area and its aperture size was also relatively small, prompting the material surface to form a large number of free channels, which makes it more conducive to lithium ions embedded in the charge and discharge process, and this unique advantages is more suitable for some of the applications related to the surface structure.

The morphologies and structural features of the samples were observed by SEM. It can be seen from Fig. S3(a–c)† that the morphology of the material C_3N_4, C_3N_4-S mainly presented a block structure, but the sample C_3N_4-B had a lamellar structure, and it can also be clearly seen that C, N, B were evenly distributed on the C_3N_4-B surface from Fig. S3(c$_1$–c$_4$).† However, after coating the composite material, ZCO@C_3N_4, ZCO@C_3N_4-S and ZCO@C_3N_4-B could be observed as mainly nanospheres, nanopieces and nanoflowers, as shown in Fig. 3(a–f). The nanoflower structure was composed of many loosely packed nanosheets and had many channel pores and a large surface area, which was also consistent with the test results from the
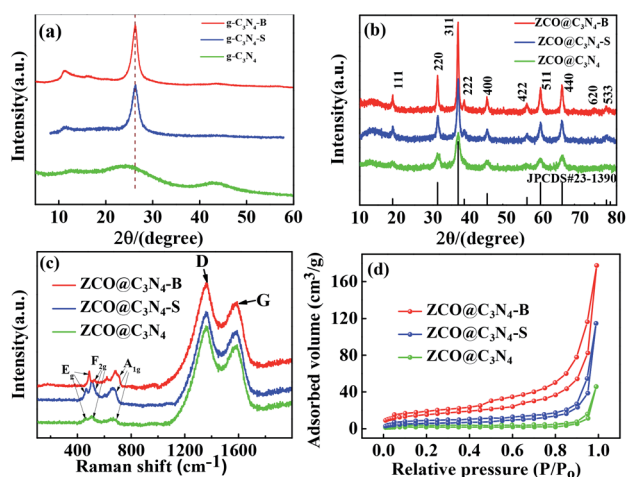

Fig. 2 (a) XRD patterns of the C_3N_4, C_3N_4-S and C_3N_4-B; (b–d) XRD patterns, Raman spectra and nitrogen adsorption–desorption of ZCO@C_3N_4, ZCO@C_3N_4-S and ZCO@C_3N_4-B.
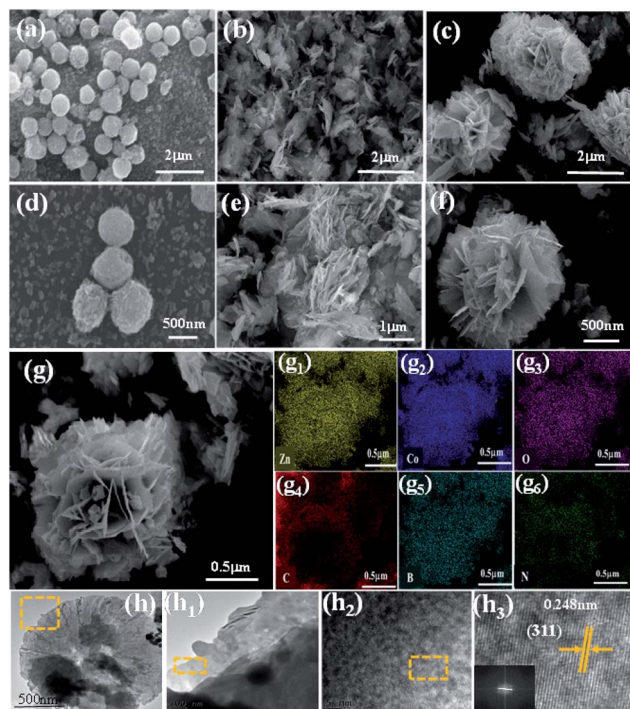
Fig. 3 SEM images of ZCO@C₃N₄ (a and d), ZCO@C₃N₄-S (b and e), ZCO@C₃N₄-B (c and f); (g–g₆) SEM images and the corresponding SEM-EDS elemental mapping of Zn, Co, O, C, B and N for the ZCO@C₃N₄-B; (h–h₃) HRTEM images of the ZCO@C₃N₄-B.
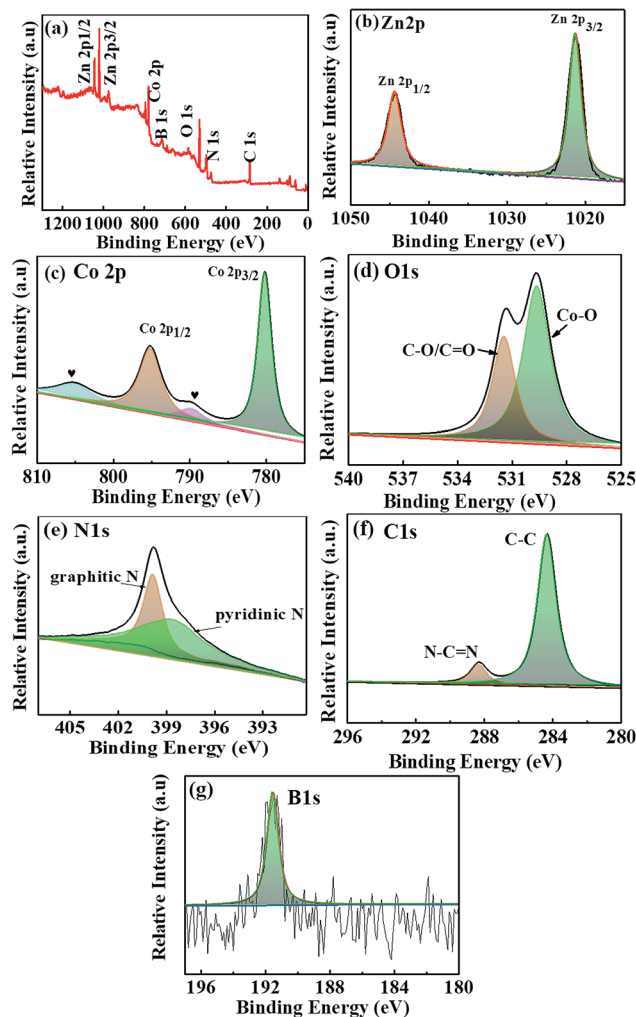

Fig. 4 (a) XPS full spectrum for the ZCO@C₃N₄-B nanoflower. (b–g) XPS high-resolution spectra of Zn 2p, Co 2p, O 1s, C 1s, N 1s and B 1s for the ZCO@C₃N₄-B.

nitrogen adsorption–desorption. At the same time, the interlaced nanosheets inside the electrodes were tightly combined, facilitating sufficient contact between the electrode/electrolyte.

The SEM-EDS mapping images of Zn, Co, O, C, B and N for ZCO@C₃N₄-B are shown in Fig. 3(g–g₆). The Zn, Co, O, C, B and N elements were uniformly distributed in the composite material. As shown in Fig. 3(h), the transmission electron microscopy (TEM) images of the nanometer flower ZCO@C₃N₄-B showed a lamellar structure (the h₁ diagram is the local enlarged diagram of Fig. 3(h)), and in the high-resolution transmission electron microscopy (HRTEM) image shown in Fig. 3(h₂), the ZCO@C₃N₄-B nanoflower visualized well-defined lattice fringes with a spacing of ~0.248 nm (shown in Fig. 3(h₃)), corresponding to the (311) crystal plane of the ZnCo₂O₄ phase.[24] Therefore, it can be concluded that the nanoflower composite material was mainly composed of (+2) Zn and (+3) Co, which strictly agrees with the above XRD results.

To further investigate the elemental composition and valence state of the ZCO@C₃N₄-B nanoflower, X-ray photoelectron spectroscopy (XPS) was performed and the results shown in Fig. 4(a) (ZCO@C₃N₄ and ZCO@C₃N₄-S shown in Fig. S1 and S2†). The strong characteristic peaks at 1086, 1021, 781, 521, 290, 502 and 714 eV correspond to Zn 2p₁/₂, Zn 2p₃/₂, Co 2p, B 1s, O 1s, C 1s and N 1s, respectively. This indicated that ZCO@C₃N₄-B was mainly composed of Zn, Co, O, C, N and B elements. There were two characteristic peaks at 1044.3 and 1020.8 eV in Fig. 4(b), corresponding to Zn 2p₁/₂ and Zn 2p₃/₂ orbitals of the Zn(II) oxidation state. The peaks of Co 2p at 795.0

and 779.7 eV were attributed to Co 2p₁/₂ and Co 2p₃/₂ orbitals in Fig. 4(c). Also, the two weaker peak at 804.3 and 789.3 eV indicated the Co(III) oxidation state of ZCO@C₃N₄-B.[7] As shown in Fig. 4(d), the peaks at 531.1 and 529.4 eV of O 1s were attributed to chemisorbed oxygen (C–O/C=O) and metal–oxygen bond (Co–O),[27] respectively. The Zn and Co elements in the calcined product ZCO@C₃N₄-B were in the form of divalent and trivalent, which were consistent with the XRD and Raman results. The large characteristic peak of C 1s at 284.3 eV represented the C–C peak of a graphene-like material, while the peak at 288.3 eV was attributed to the sp²-bonded carbon (N–C=N) in Fig. 4(e). The peaks of the graphite N and pyridine N were at 400.4 and 398.8 eV, as shown in Fig. 4(f),[18,30] respectively. As shown in Fig. 4(g), the B 1s peak at 191.6 eV was typical for C–B coordination, suggesting that B was more likely to replace N to form the C–B bond in the carbon nitride framework. This was consistent with the electronegativity principle. The binding energy of C–B should be 1–2 eV lower than N–B according to the literature.[19] Therefore, the XPS results demonstrated that B
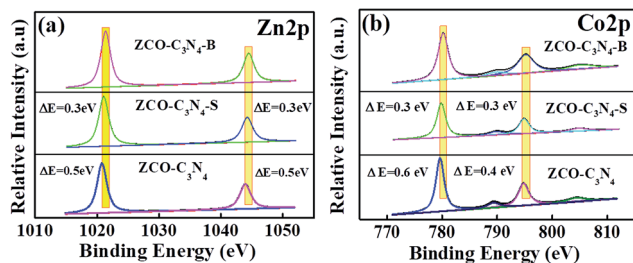
Fig. 5 (a and b) XPS spectra comparison of the Zn 2p and Co 2p spectra of ZCO@C$_3$N$_4$, ZCO@C$_3$N$_4$-S and ZCO@C$_3$N$_4$-B.

atoms successfully entered the framework of C$_3$N$_4$ and maintained the stability of the skeleton.

The high-resolution Zn 2p and Co 2p spectra of ZCO@C$_3$N$_4$, ZCO@C$_3$N$_4$-S and ZCO@C$_3$N$_4$-B are compared in Fig. 5(a and b). As shown in Fig. 5(a), compared with ZCO@C$_3$N$_4$-B, two characteristic peaks in the Zn 2p spectrum of ZCO@C$_3$N$_4$ or ZCO@C$_3$N$_4$-S showed a negative shift, indicating that the Zn(II) valence state in ZCO@C$_3$N$_4$-B was more stable. Similarly, compared to ZCO@C$_3$N$_4$-B, a slight negative shift occurred in the Co 2p peak (Fig. 5(b)) of ZCO@C$_3$N$_4$ or ZCO@C$_3$N$_4$-S. These results suggested that ZCO@C$_3$N$_4$-B was more electropositive because of the redistribution of the electron density.

3.2 Electrochemical properties

The lithium storage properties of the as-prepared ZCO@C$_3$N$_4$, ZCO@C$_3$N$_4$-S and ZCO@C$_3$N$_4$-B were investigated as the anode

Fig. 6 (a) Cycling performances of the ZCO@C$_3$N$_4$, ZCO@C$_3$N$_4$-S and ZCO@C$_3$N$_4$-B electrodes at 0.2 A g^{-1}. (b) Rate capability of the ZCO@C$_3$N$_4$, ZCO@C$_3$N$_4$-S and ZCO@C$_3$N$_4$-B electrodes at 0.2, 0.4, 0.6, 0.8, 1 and 2 A g^{-1}, respectively. (c) Capacity retention of the ZCO@C$_3$N$_4$, ZCO@C$_3$N$_4$-S and ZCO@C$_3$N$_4$-B electrodes at 0.2 A g^{-1} in different cycles (1st, 2nd, 100th, 300th and 500th). (d) Charge and discharge profiles of the ZCO@C$_3$N$_4$-B electrode for the different cycles (1st, 2nd, 100th, 300th and 500th). (e) Long-term cycling performance of the ZCO@C$_3$N$_4$-B electrode at 0.5 and 2 A g^{-1}.

in LIBs. Fig. 6(a) displays the cycling behaviour for different electrodes at 0.2 A g^{-1}. The reversible capacities of the ZCO@C$_3$N$_4$, ZCO@C$_3$N$_4$-S and ZCO@C$_3$N$_4$-B electrodes were 468.23, 616.07 and 919.76 mA h g^{-1} after 500 cycles, respectively. Comparing the three materials, the specific discharge capacity of the ZCO@C$_3$N$_4$-B electrodes increased slowly after 450 cycles, which could be the result of the reversible formation/dissolution of polymer-like gels during the transition of the metal oxide-activated electrode material.[33] While the specific capability of the other two electrodes obviously decreased gradually, which was mainly attributed to the stability of the 3D nanoflower structure of ZCO@C$_3$N$_4$-B. Meanwhile, Fig. 6(a) exhibited the almost 100% coulombic efficiency of the ZCO@C$_3$N$_4$-B electrode at a current density of 0.2 A g^{-1}. The charge–discharge properties of the electrodes at different current densities were tested and are shown in Fig. 6(b). The capacitance of the ZCO@C$_3$N$_4$-B electrode was much better than that of the other two electrodes at different current densities (0.2, 0.4, 0.6, 0.8, 1 and 2 A g^{-1}), especially at a high current density (2 A g^{-1}). Compared with ZCO@C$_3$N$_4$ and ZCO@C$_3$N$_4$-S electrodes, ZCO@C$_3$N$_4$-B retained a higher retention capacity (Fig. 6(c)). This could be because the integrity of the 3D nanoflower structure provided a shorter diffusion distance for lithium ions and enhanced the contact area between the electrolyte and graphene-like materials.[31]

Galvanostatic discharging and charging measurements were conducted to study the electrochemical performance of the ZCO@C$_3$N$_4$-B electrode. Fig. 6(d) shows the 1st, 2nd, 100th, 300th, and 500th discharge (Li$^+$ insertion) and charge (Li$^+$ extraction) profiles at a current density of 0.2 A g^{-1} in the voltage window of 0.01–3 V. The initial discharge capacity of the ZCO@C$_3$N$_4$-B electrode was 1636.34 mA h g^{-1}, which far exceeded the theoretical specific capacity of ZnCo$_2$O$_4$ (975.2 mA h g^{-1}). It decreased to 1238 mA h g^{-1} in the second cycle and the irreversible capacity loss was nearly 25%, which may be due to the formation of a solid electrolyte interface (SEI) and the reduction of the metal oxide to metal and Li$_2$O.[32] Also, the circulation capacity remained above 919 mA h g^{-1} after 500 cycles, mainly owing to the stability of the 3D flower-like structure. However, the discharge capacities of the ZCO@C$_3$N$_4$-S and ZCO@C$_3$N$_4$ electrodes were 1345.56 and 1272.26 mA h g^{-1} for the 1st cycle, respectively, and remained only at 616.53 and 468 mA h g^{-1} after 500 cycles (shown in Fig. S4†). The ZCO@C$_3$N$_4$-B electrode showed better cycle capacity than the other two electrodes. This was because the structure of the electrode was well adjusted after doping with the B element; thereby improving the electrical properties of the electrode. The voltage platform was maintained at about 0.9–1.1 V during 500 cycles discharge, suggesting that the ZCO@C$_3$N$_4$-B electrode had excellent electrochemical reversibility in lithium insertion and extraction reactions. A long cycle test of the ZCO@C$_3$N$_4$-B electrode at a high current density was performed and the result is shown in Fig. 6(e). ZCO@C$_3$N$_4$-B delivered a high reversible capacity of 686.78 mA h g^{-1} after 1000 cycles at 0.5 A g^{-1}, and maintained 95.3% capacity from the tenth cycles. In addition, a stable reversible capacity of 497.76 mA h g^{-1} at 2 A g^{-1} was obtained after 1000 cycles. These
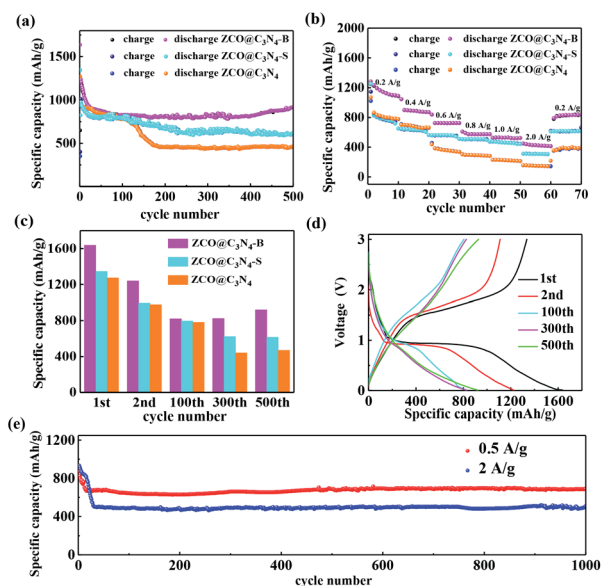
Table 1 Comparison of the electrochemical properties of $ZnCo_2O_4$-based anode materials for LIBs

Electrode material	Voltage range (V)	Current density (mA g^{-1})	Cycle number	Capacity (mA h g^{-1})	Reference
$ZnCo_2O_4$ nanocluster particles	0.005–3.0	100	100	700	5
Porous Zn–Co–O	0.01–3.0	100	200	997	6
Nanophase $ZnCo_2O_4$	0.005–3.0	60	30	900	8
ZnO/$ZnCo_2O_4$ nanocomposites	0.01–3.0	500	200	847	14
$ZnCo_2O_4$@TiO_2 nano-composite	0.01–3.0	100	90	827	15
$ZnCo_2O_4$@C_3N_4-B nanoflower	0.01–3.0	200	500	919	This work
		500	1000	686	

results showed the excellent cycling stability of the 3D nano-flower ZCO@C_3N_4-B. Furthermore, as demonstrated in Table S1,† in respect to the current rate and the cycling life, the ZCO@C_3N_4-B composite demonstrated outstanding electro-chemical properties compared to the other $ZnCo_2O_4$-based anodes for LIBs (Table 1).

To examine the electrochemical characteristics of the ZCO@C_3N_4-B electrodes, cyclic voltammetry profiles of the initial three cycles were performed and the results are displayed in Fig. 7(a). There was an intense peak at 0.31 V and a minor peak at 0.97 V in the first discharge process, which could result from the reduction of $ZnCo_2O_4$ to metallic Zn and Co and the decomposition of the electrolyte to form the SEI films, respectively. In the 2nd to 5th discharge processes, the reduction peaks were shifted to 1.52 and 1.01 V, indicating the structural modification and different lithium reaction after the first cycle. During the charge process, two oxidation peaks located at 1.82 and 2.24 V were seen, attributed to the oxidation of Zn to Zn^{2+} and CoO to Co^{3+}, respectively. The electrochemical reactions involved in the discharge and charging process could be clarified as follows:[22]
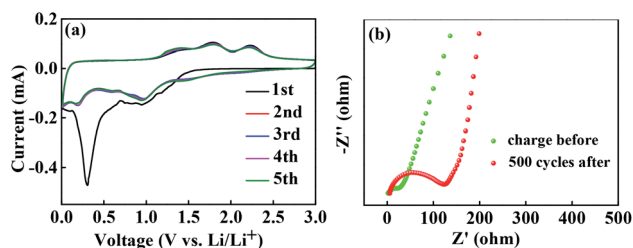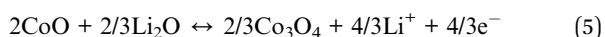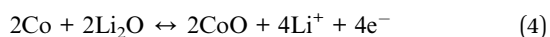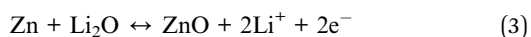
$$ZnCo_2O_4 + 8Li^+ + 8e^- \rightarrow Zn + 2Co + 4Li_2O \quad (1)$$

$$Zn + Li^+ + e^- \leftrightarrow LiZn \quad (2)$$

$$Zn + Li_2O \leftrightarrow ZnO + 2Li^+ + 2e^- \quad (3)$$

$$2Co + 2Li_2O \leftrightarrow 2CoO + 4Li^+ + 4e^- \quad (4)$$

$$2CoO + 2/3Li_2O \leftrightarrow 2/3Co_3O_4 + 4/3Li^+ + 4/3e^- \quad (5)$$

Electrochemical impedance spectroscopy (EIS) of the ZCO@C_3N_4-B electrodes before cycling and after the 500th cycle was measured and the corresponding Nyquist plots were obtained and are shown in Fig. 7(b). The Nyquist plots constituted a semicircle in the high-to-medium frequency from the charge transfer and a sloping long line in the low-frequency from the mass transfer of lithium ions. The surface layer resistance after 500 cycles ($\approx 122\ \Omega$) was very low, indicating that the ZCO@C_3N_4-B electrodes with the special flower-like structure could produce an interlaced conductive network and continuous Li^+ and e^- pathways, thus significantly enhancing the battery performance.

In order to further investigate the reason for the excellent electrochemical performance of the ZCO@C_3N_4-B electrode, the surface property of ZCO@C_3N_4-B after 500 cycles was observed by SEM (Fig. 8). After 500 cycles, the 3D nanoflower ZCO@C_3N_4-B maintained its structural integrity without cracking, leading to the excellent cycling stability. It is well known that nanostructures can provide large electrolyte contact areas and large specific surface areas, which can greatly increase the battery capacity. Also, the nanoflower structure can form a staggered conductive network and provide continuous Li^+ and e^- pathways to ensure the transfer of ions and electrons, thereby improving the long-term conductivity.
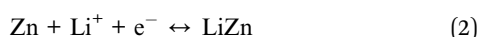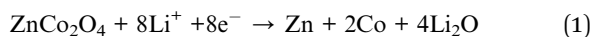

Fig. 7 (a) Cyclic voltammetry curves during the initial five cycles for the ZCO@C_3N_4-B electrode; (b) electrochemical impedance of the ZCO@C_3N_4-B electrodes after 500 cycles and the charge before.
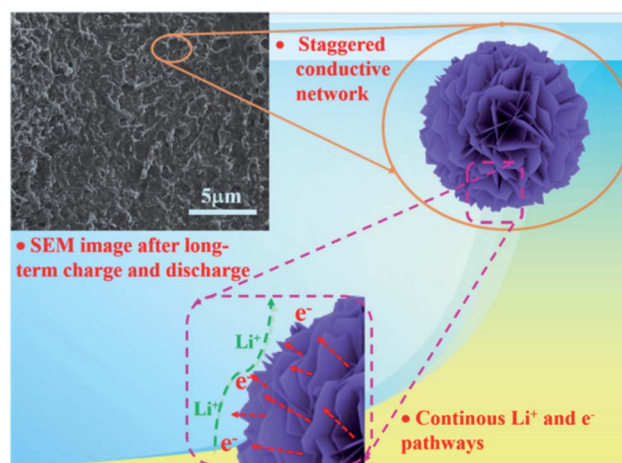

Fig. 8 Mechanism explanations of the excellent electrochemical performance of the nanoflower ZCO@C_3N_4-B electrode.

4. Conclusion

In summary, a special three-dimensional (3D) nanoflower ZCO@C$_3$N$_4$-B was successfully synthesized using a simple hydrothermal method. At a current density of 0.2 A g^{-1}, the nanoflower electrode capacity remained above 919 mA h g^{-1} after 500 cycles. Also, it displayed excellent cycling stability at 0.5 A g^{-1} and 2 A g^{-1} after 1000 cycles. The excellent electrochemical performance of the ZCO@C$_3$N$_4$-B electrode was attributed to its steady special secondary structure, integrated staggered conductive network, large electrolyte contact area and continuous lithium ion and electron pathways. The nanoflower ZCO@C$_3$N$_4$-B has potential to serve as an anode material for lithium-ion batteries and is expected to be used in industrial applications.

Conflicts of interest

The authors declare no competing financial interest.

Acknowledgements

Notes and references

1 Z. Yang, J. Ren, Z. Zhang, X. Chen, G. Guan, L. Qiu, Y. Zhang and H. Peng, *Chem. Rev.*, 2015, **115**, 5159–5223.
2 B. Saparov and D. B. Mitzi, *Chem. Rev.*, 2016, **116**, 4558–4596.
3 Z. Zhao-Karger, P. Gao, T. Ebert, S. Klyatskaya, Z. Chen, M. Ruben and M. Fichtner, *Adv. Mater.*, 2019, **31**, 1806599.
4 S. Zheng, X. Li, B. Yan, Q. Hu, Y. Xu, X. Xiao, H. Xue and H. Pang, *Adv. Energy Mater.*, 2017, **7**, 1602733.
5 Y. Pan, W. Zeng, L. Li, Y. Zhang, Y. Dong, D. Cao, G. Wang, B. L. Lucht, K. Ye and K. Cheng, *Nano-Micro Lett.*, 2016, **9**, 3–9.
6 M. H. Soo, Y. K. So, J.-G. Kim, Ki J. Kim, J.-W. Lee, M.-S. Park, Y.-J. Kim, M. Shahabuddin, Y. Yamauchi and J. Ho Kim, *Nanoscale*, 2015, **7**, 8351–8355.
7 K. N. Jung, S. M. Hwang, M. S. Park, Ki J. Kim, J. Kim, S. X. Dou, J. Ho Kim and J. Lee, *Sci. Rep.*, 2015, **5**, 7665.
8 Y. Sharma, N. Sharma, G. V. Subba Rao and B. V. R. Chowdari, *Adv. Energy Mater.*, 2007, **17**, 2855–2861.
9 R. Zhao, Q. Li, C. Wang and L. Yin, *Electrochim. Acta*, 2016, **197**, 58–67.
10 Y. Wang, W. Guo, Y. Yang, Y. Yu, Q. Li, D. Wang and F. Zhang, *Electrochim. Acta*, 2018, **262**, 1–8.
11 A. W. Nemaga, J. Mallet, J. Michel, C. Guery, M. Molinari and M. Morcrette, *J. Power Sources*, 2018, **393**, 43–53.
12 Y. Ouyang, H. Ye, X. Xia, X. Jiao, G. Li, S. Mutahir, L. Wang, D. Mandler, W. Lei and Q. Hao, *J. Mater. Chem. A*, 2019, **7**, 3228–3237.

13 J. B. Boland, A. Harvey, R. Tian, D. Hanlon, V. Vega-Mayoral, B. Szydlowska, A. Griffin, T. Stimpel-Lindner, S. Jaskaniec, V. Nicolosi, G. Duesberg and J. N. Coleman, *Nanoscale Adv.*, 2019, **1**, 1560–1570.
14 J. Xu, L. He, Y. Wang, C. Zhang and Y. Zhang, *Electrochim. Acta*, 2016, **191**, 417–425.
15 W. Shi, H. Zhao and B. Lu, *Nanotechnology*, 2017, **28**, 165403.
16 X. Cheng, D. Li, Y. Wu, R. Xu and Y. Yu, *J. Mater. Chem. A*, 2019, **7**, 4913–4921.
17 G. Wang, Z. Wen, Y.-E. Yang, J. Yin, W. Kong, S. Li, J. Sun and S. Ji, *J. Mater. Chem. A*, 2018, **6**, 7557–7565.
18 H. Yang, Y. Zhou, Y. Wang, S. Hu, B. Wang, Q. Liao, H. Li, J. Bao, G. Ge and S. Jia, *J. Mater. Chem. A*, 2018, **6**, 16485–16494.
19 H. Yu, X. Jiang, Z. Shao, J. Feng, X. Yang and Y. Liu, *Nanoscale Res. Lett.*, 2018, **13**, 52–57.
20 Q. Yan, G.-F. Huang, D.-F. Li, M. Zhang, A.-L. Pan and W.-Q. Huang, *J. Mater. Sci. Technol.*, 2018, **34**, 2515–2520.
21 Y. Wang, Y. Li, J. Zhao, J. Wang and Z. Li, *Int. J. Hydrogen Energy*, 2019, **44**, 618–628.
22 Y. V. Kaneti, N. L. Wulan Septiani, I. Saptiama, X. Jiang, B. Yuliarto, M. J. A. Shiddiky, N. Fukumitsu, Y.-M. Kang, D. Golberg and Y. Yamauchi, *J. Mater. Chem. A*, 2019, **7**, 3415–3425.
23 R. Ding, J. Zhang, J. Qi, Z. Li, C. Wang and M. Chen, *ACS Appl. Mater. Interfaces*, 2018, **10**, 13470–13478.
24 M. Liu, Z. Zhang, M. Dou, Z. Li and F. Wang, *Carbon*, 2019, **151**, 28–35.
25 Y. Xiao, G. Tian, W. Li, Y. Xie, B. Jiang, C. Tian, D. Zhao and H. Fu, *J. Am. Chem. Soc.*, 2019, **141**, 2508–2515.
26 Y. Wang, M. Wang, G. Chen, C. Dong, Y. Wang and L.-Z. Fan, *Ionics*, 2014, **21**, 623–628.
27 Q. Li, Y. Feng, P. Wang and R. Che, *Nanoscale*, 2019, **11**, 5080–5093.
28 J. Li, X. Li, L. Zeng, S. Fan, M. Zhang, W. Sun, X. Chen, M. O. Tade and S. Liu, *Nanoscale*, 2019, **11**, 3877–3887.
29 Z. Chen, C. Wang, M. Chen, C. Ye, Z. Lin, L. Xing, Y. Liao, M. Xu, G. Cao and W. Li, *J. Mater. Chem. A*, 2019, **7**, 3924–3932.
30 H. Che, A. Liu, X. Zhang, J. Mu, Y. Bai and J. Hou, *Ceram. Int.*, 2015, **41**, 7556–7564.
31 R. Fang, K. Chen, L. Yin, Z. Sun, F. Li and H. M. Cheng, *Adv. Mater.*, 2019, **31**, 1800863.
32 J. Zhou, B. Zhao and J. Bai, *Scr. Mater.*, 2019, **166**, 87–91.
33 Y. R. Zhang, Z. L. Wang, F. uz Zaman, Z. W. Zhao, X. Sun, J. Y. Zhang, L. R. Hou and C. Z. Yuan, *J. Mater. Chem. A*, 2019, **7**, 3264–3277.
34 A. P. Wang, S. Kadam, H. Li, S. Q. Shi and Y. Qi, *npj Comput. Mater.*, 2018, **4**, 34–39.
35 J. J. Zhang and A. S. Yu, *Sci. Bull.*, 2015, **60**, 823–838.
36 N. Vicente and G. Garcia-Belmonte, *J. Phys. Chem. Lett.*, 2017, **8**, 1371–1374.